



## Ru nanoassembly catalysts for hydrogen evolution and oxidation reactions in electrolytes at various pH values



Yuzhi Li<sup>a</sup>, Janel Abbott<sup>b</sup>, Yanchun Sun<sup>c</sup>, Jianmin Sun<sup>a</sup>, Yunchen Du<sup>a</sup>, Xijiang Han<sup>a</sup>, Gang Wu<sup>b,\*</sup>, Ping Xu<sup>a,\*</sup>

<sup>a</sup> MIIT Key Laboratory of Critical Materials Technology for New Energy Conversion and Storage, School of Chemistry and Chemical Engineering, Harbin Institute of Technology, Harbin 150001, China

<sup>b</sup> Department of Chemical and Biological Engineering, University at Buffalo, The State University of New York, Buffalo, New York, 14260, United States

<sup>c</sup> Heilongjiang River Fisheries Research Institute of Chinese Academy of Fishery Sciences, Laboratory of Quality & Safety Risk Assessment for Aquatic Products (Harbin), Ministry of Agriculture, Harbin 150070, China

### ARTICLE INFO

#### Keywords:

Ru nanoassembly  
Electrocatalysts  
HER  
HOR  
Reversible fuel cells

### ABSTRACT

Here, in an effort to prepare Ru-based metal organic frameworks, we developed a one-step solvothermal synthesis for Ru nanoassembly catalysts, which consist of ~4 nm Ru nanoparticles well dispersed on amorphous carbon (Ru/C). The Ru/C catalyst obtained from a mixed solvent of H<sub>2</sub>O and CH<sub>3</sub>CH<sub>2</sub>OH (Ru/C-H<sub>2</sub>O/CH<sub>3</sub>CH<sub>2</sub>OH), featured a chain-like porous structure, provides Pt-like catalytic properties with low overpotentials at ~10 mA cm<sup>-2</sup> for the hydrogen evolution reaction (HER) within a wide range of pH values, i.e., 35 mV in 0.5 M H<sub>2</sub>SO<sub>4</sub>, 53 mV in 1.0 M KOH, and 93 mV in 3.5 wt% NaCl. Ru/C is also an efficient hydrogen oxidation reaction (HOR) catalyst at all pH values. In the alkaline media, Ru/C-H<sub>2</sub>O/CH<sub>3</sub>CH<sub>2</sub>OH achieves a mass activity of 41.1 mA mg<sup>-1</sup> at an overpotential of 50 mV and a high exchange current density (0.65 mA cm<sup>-2</sup>). The work provides a facile strategy to synthesize highly active Ru/C catalysts for bifunctional HER and HOR electrocatalysis.

### 1. Introduction

The intensifying energy crisis and corresponding environmental impacts have stimulated enormous interests in developing a clean, renewable, highly-efficient energy source [1–4]. Hydrogen is one of the most promising energy sources to replace traditional fossil fuels [5–7]. Among various possible techniques, electrochemical water splitting reveals an efficient and suitable alternative for hydrogen production [8–12]. Boosting the efficiency and lowering the overpotential of hydrogen evolution reaction (HER) and its reverse, hydrogen oxidation reaction (HOR), is of great importance for efficiently utilizing hydrogen energy. However, the overall efficiency of energy conversion devices is rigorously hindered by the sluggish kinetics of these electrocatalytic reactions [6,13–16].

To date, Pt-based compounds are still the most efficient electrocatalysts for the HER and HOR. Unfortunately, high cost and scarcity preclude precious metal catalysts for large-scale applications [17–21]; it remains urgent to develop low-Pt or Pt-free catalysts with excellent activity and stability for the above-mentioned reactions. Ru is a member of the precious metal family, but is 10 times lower in price than

Pt. Ru-based materials are widely recognized for their high oxygen evolution reaction (OER) activity [22,23], and theoretically they are also ideal HER catalysts due to the favorable Ru-H bond strength and the ability to lower the barrier to hydrogen desorption [23,24], which might be operated under both acidic and alkaline conditions [25–27]. Recent advances suggested that Ru and Ru-based composites can provide electrocatalytic activities comparable to commercial Pt/C [28–32], an indication that Ru-related materials might be promising candidates for hydrogen reactions. However, it needs to be pointed out that the synthesis routes for most Ru-based materials usually require a high-temperature carbothermal reduction process, and thus a facile synthesis strategy is being pursued.

Metal-organic frameworks (MOFs) can be directly converted into metal-decorated carbon nanocomposites with high specific surface area and highly dispersed metal centers through a pyrolysis process under an inert atmosphere [13,33–36]. Recent works have reported the synthesis and catalytic properties of Ru-MOFs [37–39], however, there are few reports on their applications to HER and HOR. Herein, in an effort to synthesize a self-supported Ru/C catalyst from Ru-MOFs, we readily obtained Ru nanoassemblies consisting of ~4 nm Ru nanoparticles

\* Corresponding authors.

E-mail addresses: [gangwu@buffalo.edu](mailto:gangwu@buffalo.edu) (G. Wu), [pxu@hit.edu.cn](mailto:pxu@hit.edu.cn) (P. Xu).

supported on a carbon matrix (Ru/C) during the solvothermal synthesis of Ru-MOFs. The size of Ru nanoparticles and the assembly process strongly depend on the solvents used during the synthesis procedure. With a mixture of water and ethanol as the solvent, the as-prepared Ru/C-H<sub>2</sub>O/CH<sub>3</sub>CH<sub>2</sub>OH provides very encouraging HER performance, which can achieve -10 mA cm<sup>-2</sup> at a low overpotential of 35, 53, and 93 mV in acidic, alkaline and neutral media, respectively. The HOR electrocatalytic activity of Ru/C-H<sub>2</sub>O/CH<sub>3</sub>CH<sub>2</sub>OH is comparable to Pt/C with a high mass activity of 21.9, 41.1 and 2.7 mA mg<sup>-1</sup> at 50 mV overpotential in acidic, alkaline and neutral media, respectively. This one-pot synthetic strategy for Ru-based materials may provide new possibilities for the development of scalable, durable and superior electrocatalysts for sustainable energy conversion technology.

## 2. Experimental section

### 2.1. Materials and chemicals

All the reagents and solvents used for the synthesis were commercially available and used without further purification. 1,3,5-Benzenetricarboxylic acid (H<sub>3</sub>BTC, Sigma Aldrich, 98%), ruthenium(III) chloride hydrate (RuCl<sub>3</sub>·xH<sub>2</sub>O, MW = 207.43, 35–42%), acetic acid (HAc) and ruthenium powder (99.9%) were purchased from Aladdin Reagent. Absolute ethyl alcohol (CH<sub>3</sub>CH<sub>2</sub>OH, ≥99.5%) was purchased from Sinopharm Chemical Reagent Co. Ltd. and commercial Pt/C (20% Pt on Vulcan XC-72) was purchased from Alfa Aesar. Deionized (DI) water from MilliQ system, (18 MΩ cm) was used in all experiments.

### 2.2. Synthesis of Ru/C

Ru/C samples were prepared according to a previous report on manufacturing Ru-MOFs materials with slight modification [40]. In a typical synthesis procedure, RuCl<sub>3</sub>·xH<sub>2</sub>O (3 mmol) and HAc (286 μL, 5 mmol) were dissolved in 8.4 mL deionized (DI) water under magnetic stirring to form a homogeneous solution, followed by an addition of H<sub>3</sub>BTC (2 mmol) dissolved in 8.4 mL of ethanol. The solution was transferred to a 50 mL Teflon-lined autoclave and kept in a 160 °C oven for 72 h. After cooling down to room temperature, the final product was collected by centrifugation, washed with DI water then ethanol and dried under vacuum at 60 °C for 12 h. This sample was designated as Ru/C-H<sub>2</sub>O/CH<sub>3</sub>CH<sub>2</sub>OH. In the control experiments, Ru/C samples were synthesized with either only water or ethanol as the solvent, and the products were named as Ru/C-H<sub>2</sub>O and Ru/C-CH<sub>3</sub>CH<sub>2</sub>OH, respectively.

### 2.3. Characterizations

Powder X-ray diffraction (PXRD) data were recorded on a Rigaku D/MAXRC X-ray diffractometer (45.0 kV, 50.0 mA) using Cu target as the anticathode. The thermogravimetric analysis (TGA) was carried out on an SDT Q600 TGA (TA Instruments) in the temperature range of 25 °C–800 °C at a heating rate of 10 °C/min. Scanning electron microscopic (SEM) images were obtained on a Quanta 200 S (FEI), and transmission electron microscopic (TEM) images were obtained on a Tecnai F20 operating at an accelerating voltage of 200 kV. The Raman spectra were collected on a Renishaw in Via micro Raman spectroscopy system, using the TE air-cooled 576 × 400 CCD array in a confocal Raman system (wavelength: 532 nm). The incident laser power was kept at 0.1 mW, and a total accumulation time of 10 s were employed. X-ray photoelectron spectra (XPS) was obtained with PHI 5700 ESCA system equipped with an Al Kα radiation as a source ( $\hbar\omega = 1486.6$  eV). Nitrogen adsorption-desorption isotherms were obtained on a QUAD-RASORB SI-KR/MP (Quantachrome, USA).

## 2.4. Electrode preparation and electrochemical characterization

### 2.4.1. Electrode preparation

The catalyst ink was prepared by dispersing 4.0 mg catalyst or commercial Pt/C (20 wt %) powder into a dispersant composed of 5 μL 5 wt% Nafion solution as a binder and 800 μL water-ethanol solution (v/v, 1:3) with the assistance of sonication for at least 1 h. The working electrodes were prepared by dropping 7.5 μL catalyst ink onto a glassy-carbon disk with a geometric area of 0.196 cm<sup>2</sup>, yielding an estimated catalyst loading of  $0.19 \pm 0.01$  mg/cm<sup>2</sup>, corresponding to a metal loading of 0.15, 0.17, 0.17, 0.18 mg<sub>Ru</sub> cm<sup>-2</sup> for Ru/C-H<sub>2</sub>O, Ru/C-H<sub>2</sub>O/CH<sub>3</sub>CH<sub>2</sub>OH, Ru/C-CH<sub>3</sub>CH<sub>2</sub>OH and Ru powder, respectively. A loading of 0.04 mg<sub>Pt</sub> cm<sup>-2</sup> was used for commercial Pt/C. In order to eliminate the errors caused by ink preparation, fresh-made ink was used during the electrochemical measurements and average values were provided based on three measurements. All the electrochemical measurements were carried out on an electrochemical workstation CHI 660D (CH Instruments, Inc.) in a standard three-electrode cell with a glassy carbon electrode (GCE, 5 mm in diameter) as the working electrode (WE) and a graphite rod (Alfa Aesar, 99.9995%) as the counter electrode (CE). A saturated Hg/Hg<sub>2</sub>SO<sub>4</sub> electrode (in saturated K<sub>2</sub>SO<sub>4</sub> solution) was used as the reference electrode in acidic solution, and an Ag/AgCl electrode (in 3.5 M KCl solution) was used as the reference electrode in alkaline and neutral medium. 0.5 M H<sub>2</sub>SO<sub>4</sub>, 1.0 M KOH, and 3.5 wt% NaCl aqueous solutions were used as the acidic, alkaline, and neutral electrolytes, respectively. The WE was first cycled for 50 cycles at 50 mV s<sup>-1</sup> in the corresponding electrolyte solution. All the potentials were referred to RHE. All current densities were normalized to the geometric area of the glassy carbon disk. For all the electrochemical measurements, the corresponding electrolytes were saturated with H<sub>2</sub> by continuous purging with high-purity H<sub>2</sub> (99.999%) during the measurement processes.

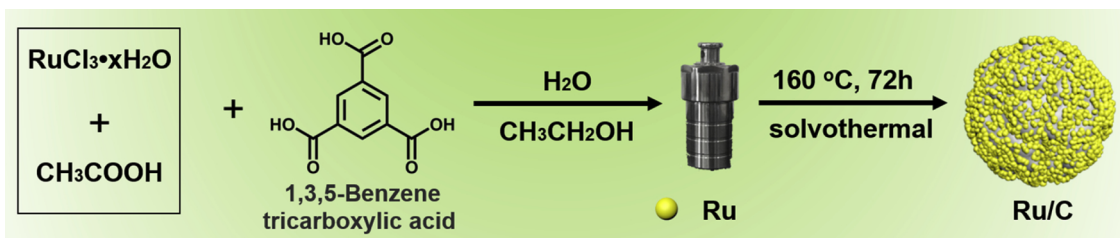
### 2.4.2. HER measurements

Linear sweep voltammetry (LSV) was recorded at a scan rate of 2 mV s<sup>-1</sup> at room temperature. Cyclic voltammograms (CV) in the 0.1–0.2 V range were collected at various scan rates (20, 40, 60, 80, 100, 120, 140, 160, 180 and 200 mV/s) and used to estimate the double-layer capacitance ( $C_{dl}$ ). The electrochemical impedance spectroscopy (EIS) measurements were carried out at an overpotential of 110 mV with the frequency ranging from 10<sup>6</sup> to 0.1 Hz. To compare the intrinsic catalytic activity of the different catalysts, we used the series resistance (~5 Ω) determined from EIS experiments to correct the polarization measurements and subsequent Tafel analysis for the *iR* losses. The stability tests of the studied catalysts were conducted at a constant overpotential for achieving a high initial current density.

### 2.4.3. HOR measurements

The HOR electrocatalytic testing was carried out in a H<sub>2</sub>-purged 0.1 M HClO<sub>4</sub>, 0.1 M KOH and 3.5 wt% NaCl aqueous solutions using a three-electrode cell. The CV was recorded in N<sub>2</sub>-saturated HClO<sub>4</sub>/KOH /3.5 wt% NaCl solution between -0.1 and 1.2 V at a scan rate of 50 mV s<sup>-1</sup>. After the electrolyte was saturated with pure hydrogen for at least 30 min, the HOR polarization curves were measured by sweeping the potential from -0.1 to 1.0 V at a scan rate of 10 mV s<sup>-1</sup> under different rotation rates (400, 900, 1600, 2500 and 3600 rpm).

Cu<sub>upd</sub> stripping voltammetry (0.3–0.9 V, 10 mV s<sup>-1</sup>) was performed in a N<sub>2</sub>-purged 0.1 M HClO<sub>4</sub> solution containing 2 mM Cu(ClO<sub>4</sub>)<sub>2</sub> at 25 °C after Cu deposition at 0.3 V versus RHE for 100 s. Before the voltammetry, the catalysts were pretreated by CV (0.1–1 V, 500 mV s<sup>-1</sup>, 100 cycles) in 0.1 M HClO<sub>4</sub> solution without Cu(ClO<sub>4</sub>)<sub>2</sub>. For Ru/C, further CV pretreatment (0–0.01 V, 0.1 mV s<sup>-1</sup>) was carried out until the voltammogram did not change. The voltammogram on each catalyst in 0.1 M HClO<sub>4</sub> solution without Cu(ClO<sub>4</sub>)<sub>2</sub> (0.3–0.9 V, 10 mV s<sup>-1</sup>) was applied as the background for the corresponding Cu<sub>upd</sub> stripping voltammogram.



**Scheme 1.** Schematic illustration for the synthesis of Ru/C nanoassemblies through a solvothermal process.

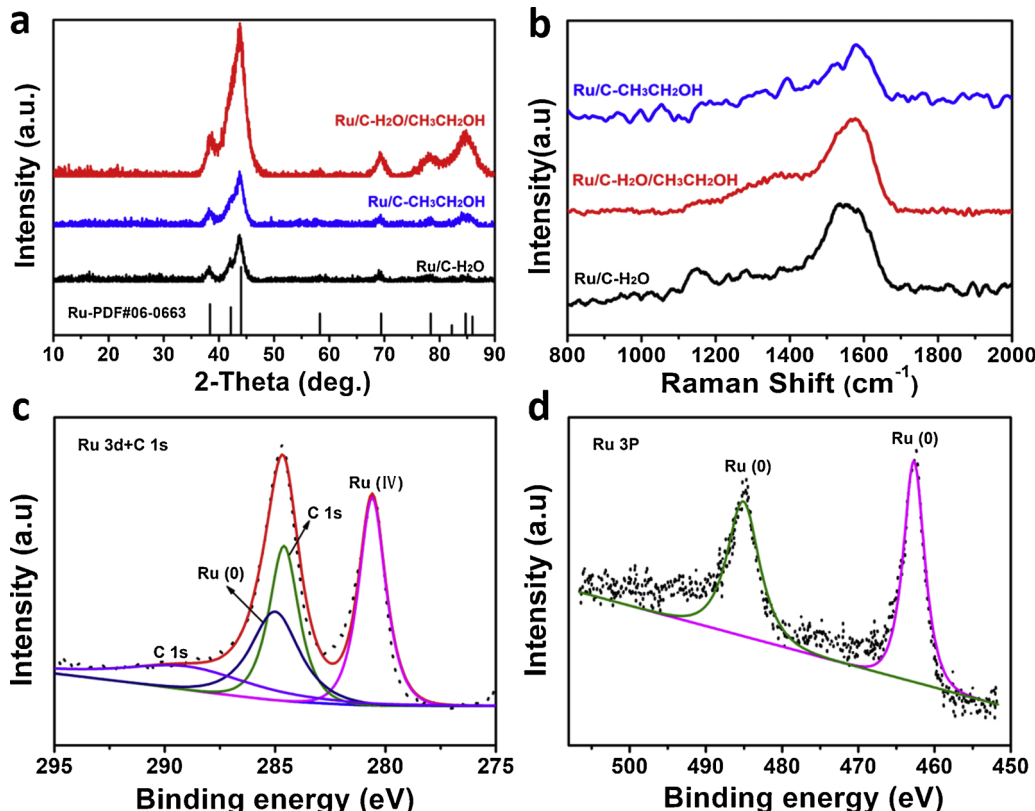


**Fig. 1.** (a) XRD patterns and (b) Raman spectra of Ru/C-H<sub>2</sub>O, Ru/C-H<sub>2</sub>O/CH<sub>3</sub>CH<sub>2</sub>OH and Ru/C-CH<sub>3</sub>CH<sub>2</sub>OH. XPS spectra of (c) Ru 3d + C 1s and (d) Ru 3p levels of Ru/C-H<sub>2</sub>O/CH<sub>3</sub>CH<sub>2</sub>OH.

### 3. Results and discussion

In an attempt to prepare Ru-MOFs featuring the HKUST-1 structure type with the presence of H<sub>3</sub>BTC [41,42], a Ru nanoassembly supported on a carbon matrix (**Scheme 1**) was obtained, regardless of the solvent used during the solvothermal process (H<sub>2</sub>O and/or CH<sub>3</sub>CH<sub>2</sub>OH). The formation of Ru in different reaction systems can be strongly supported by PXRD (**Fig. 1a**), where the well-resolved diffraction peaks at  $2\theta = 38.3, 42.1, 44.0, 58.3, 69.4, 78.3, 82.2, 84.7$ , and  $85.9^\circ$  can be indexed to the (100), (002), (101), (102), (110), (103), (200), (112), and (201) planes of metallic Ru with hcp crystalline structure (JCPDS 06-0663: P63/mmc (194)), respectively. However, no other peaks assigned to carbon can be observed, which may be due to the low content and amorphous feature of carbon in the formed Ru/C [43]. The average particle size calculated by the Scherrer equation from fitting the peak of the Ru (101) plane is 3.9, 3.2 and 3.7 nm for Ru/C-H<sub>2</sub>O, Ru/C-H<sub>2</sub>O/CH<sub>3</sub>CH<sub>2</sub>OH and Ru/C-CH<sub>3</sub>CH<sub>2</sub>OH, respectively. Raman spectra (**Fig. 1b**) reveals that all Ru/C samples contain poorly crystallized carbon materials [44,45]. Above results clearly suggest the production of Ru/C nanocomposites through our solvothermal routes. In order to understand the formation mechanism, we tried several control experiments without the addition of HAc and/or H<sub>3</sub>BTC. PXRD results showed

that elemental Ru could be also produced (**Fig. S1**). Moreover, Ru can be formed simply with only RuCl<sub>3</sub>·xH<sub>2</sub>O and deionized water in the solvothermal system (**Fig. S2**). It should be pointed out that without H<sub>3</sub>BTC, carbon materials could not be formed (**Fig. S3**). It is found in our experiments that H<sub>3</sub>BTC is slightly soluble in water at room temperature, and thus in this solvothermal synthesis process, RuCl<sub>3</sub>·xH<sub>2</sub>O first self-decomposes into Ru nanoparticles in an acetic acid aqueous solution before complexing with H<sub>3</sub>BTC. This result indicates that H<sub>3</sub>BTC, a ligand for Ru-MOFs, is the carbon source and stabilizer during the formation of Ru/C nanocomposites.

To further investigate the species in surface layers of Ru/C nanocomposites, XPS was carried out. **Fig. S4** shows the XPS survey spectrum of Ru/C-H<sub>2</sub>O/CH<sub>3</sub>CH<sub>2</sub>OH, where three elements including C, O and Ru were detected. The elemental contents (atom %) derived from XPS are shown in Table S1, where the Ru and carbon content is about 58.22% and 35.38%, respectively. As shown in the Ru 3d + C 1s spectrum (**Fig. 1c**) of Ru/C-H<sub>2</sub>O/CH<sub>3</sub>CH<sub>2</sub>OH, the Ru 3d<sub>5/2</sub> core-line has a binding energy of 281.3 eV, due to the existence of RuO<sub>2</sub> [46], which originates from the formation of an oxide passivation layer due to air exposure of the nanomaterial during XPS analysis. As reported [47,48], the peak near 281 eV can be ascribed to the Ru 3d<sub>3/2</sub> of Ru<sup>0</sup> and the peak at 284.6 eV corresponds more likely to the C 1s of poorly

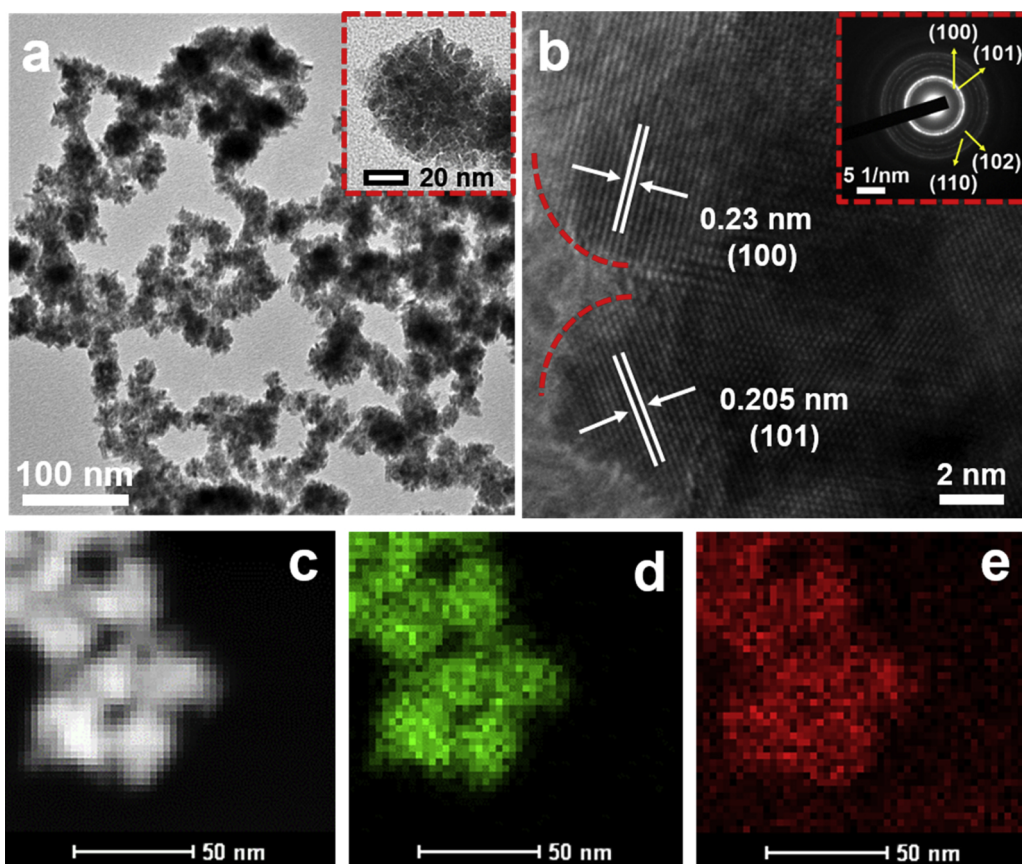


**Fig. 2.** (a) TEM image of Ru/C-H<sub>2</sub>O/CH<sub>3</sub>CH<sub>2</sub>OH (inset shows a single nanoassembly), (b) HRTEM image of Ru/C-H<sub>2</sub>O/CH<sub>3</sub>CH<sub>2</sub>OH (inset shows the corresponding SAED pattern), (c) STEM image of Ru/C-H<sub>2</sub>O/CH<sub>3</sub>CH<sub>2</sub>OH and the corresponding EDX elemental mapping of (d) Ru and (e) C.

crystallized carbon species. As for the Ru 3p peaks (Fig. 1d), two component peaks at 462.6 eV and 484.9 eV are observed, which can be attributed to Ru 3p<sub>3/2</sub> and Ru 3p<sub>1/2</sub> of Ru<sup>0</sup>, respectively [25,49–51]. These results also confirm the presence of metallic Ru and C in the surface of the as-synthesized Ru/C nanocomposites.

The morphology features of the prepared samples were studied by transmission electron microscopy (TEM). As shown in Fig. 2a, the as-prepared chain-like Ru/C-H<sub>2</sub>O/CH<sub>3</sub>CH<sub>2</sub>OH is composed of loosely assembled Ru nanoparticles supported on a carbon matrix. More detailed investigation of assembled structures (inset in Fig. 2a) indicates that these nanoparticles display a sponge-like morphology and the Ru nanoparticles are uniformly distributed with an average size of about 4 nm (Fig. S5). This loose structure endows Ru/C-H<sub>2</sub>O/CH<sub>3</sub>CH<sub>2</sub>OH with a large specific surface area and more exposed Ru nanoparticles, which are two important characteristics for high catalytic activity. High resolution TEM (HRTEM) image (Fig. 2b) shows clear lattice fringes of 0.230 and 0.205 nm, corresponding to the (100) and (101) plane of Ru with hcp structure, respectively. Furthermore, the elemental mapping from the scanning transmission microscopic (STEM) image in Fig. 2c further confirms that such assembled structures are formed by the uniform distribution of Ru nanoparticles in the carbon matrix (Fig. 2d, e). Here, the lattice fringe of carbon cannot be detected due to its amorphous nature. With only ethanol as the solvent (denoted as Ru/C-CH<sub>3</sub>CH<sub>2</sub>OH), Ru nanoparticles have fast nucleation rate, high energy and instability, so small nanoparticles tend to attach to each other and assemble to form dense spheres that are about 50 nm to 100 nm in overall size (Fig. S6a). With only water as the solvent (Ru/C-H<sub>2</sub>O), more compact and larger spheres are obtained (Fig. S6b). The morphological differences of Ru/C nanocomposites formed in different systems are mainly due to the low solubility of H<sub>3</sub>BTC in water, which probably affects the formation of carbon matrix as well as the Ru nanoparticle

growth. Thus, ethanol was used together with water for dissolving H<sub>3</sub>BTC in the experiments for better morphology control. N<sub>2</sub> adsorption-desorption isotherms were collected in Fig. S7a. BET surface areas are calculated as 1.51, 61.48 and 4.34 m<sup>2</sup> g<sup>-1</sup> for Ru/C-H<sub>2</sub>O, Ru/C-H<sub>2</sub>O/CH<sub>3</sub>CH<sub>2</sub>OH and Ru/C-CH<sub>3</sub>CH<sub>2</sub>OH, respectively. It is also revealed that Ru/C-H<sub>2</sub>O/CH<sub>3</sub>CH<sub>2</sub>OH has a porous feature, with a pore size centered at 4.7 nm (Fig. S7b), while Ru/C-H<sub>2</sub>O and Ru/C-CH<sub>3</sub>CH<sub>2</sub>OH do not have significant porous structures. This also implies that the morphology and structure of the Ru/C nanocomposites can be effectively manipulated by the solvent used during the solvothermal synthesis. TG analysis was utilized to determine the specific Ru content in the Ru/C nanocomposites. By considering that the oxidation of Ru into RuO<sub>2</sub> will compensate for the combustion of carbon species, the Ru content should be estimated according to the following equation:

$$\text{wt\% Ru} = (\text{wt\% R}) \frac{M(\text{Ru})}{M(\text{RuO}_2)}$$

where wt% R is the remaining weight percentage after combustion, and M refers to the molecular weight. The calculation results indicate that the Ru content of Ru/C-H<sub>2</sub>O, Ru/C-H<sub>2</sub>O/CH<sub>3</sub>CH<sub>2</sub>OH and Ru/C-CH<sub>3</sub>CH<sub>2</sub>OH are about 82.8, 91.44, and 90.6 wt%, respectively (Fig. S8).

The electrocatalytic HER performance of Ru/C-H<sub>2</sub>O, Ru/C-H<sub>2</sub>O/CH<sub>3</sub>CH<sub>2</sub>OH and Ru/C-CH<sub>3</sub>CH<sub>2</sub>OH was investigated in acidic, alkaline, and neutral media using a rotating ring disk electrode (RDE) with a 1600 rpm rotation rate. Commercial Ru powder and 20% Pt/C are shown for comparison. The catalysts were drop cast onto a GCE. Fig. 3a shows the iR corrected cathodic-sweeping polarization curves of these catalysts in 0.5 M H<sub>2</sub>SO<sub>4</sub>. The Ru/C-H<sub>2</sub>O/CH<sub>3</sub>CH<sub>2</sub>OH displays an efficient catalytic activity with a low overpotential of 35 mV at a current density of -10 mA cm<sup>-2</sup> ( $\eta_{10} = 35$  mV), significantly outperforming the Ru/C-H<sub>2</sub>O ( $\eta_{10} = 60$  mV) and Ru/C-CH<sub>3</sub>CH<sub>2</sub>OH ( $\eta_{10} = 66$  mV). This

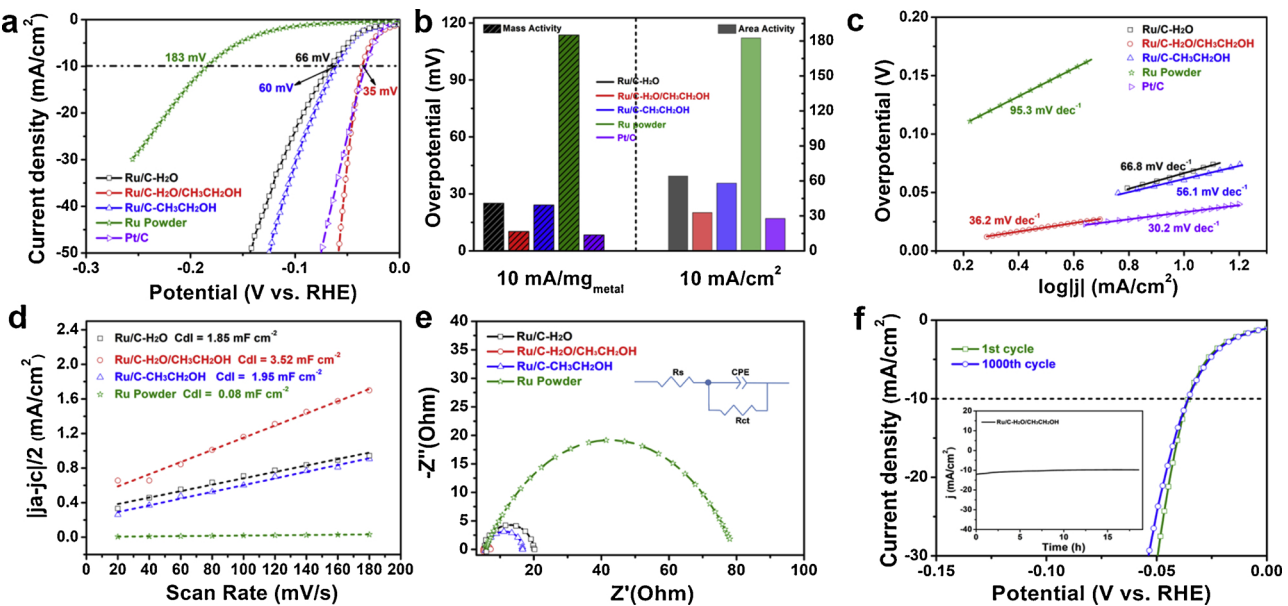


**Fig. 3.** Electrochemical characterization of the Ru/C nanoassemblies for HER catalysis in 0.5 M H<sub>2</sub>SO<sub>4</sub>. (a) Polarization curves after *iR* correction, in comparison to Pt/C and Ru powder. (b) Overpotential of samples at 10 mA mg<sub>metal</sub><sup>-1</sup> and 10 mA cm<sup>-2</sup>. (c) Tafel plots for the data presented in (a). (d) Plots showing the extraction of the C<sub>dl</sub>. (e) Electrochemical impedance spectroscopy (inset shows the equivalent circuit used to simulate the Nyquist plots). (f) Polarization curves of Ru/C-H<sub>2</sub>O/CH<sub>3</sub>CH<sub>2</sub>OH at the 1st and 1000th cycle. Inset is stability of Ru/C-H<sub>2</sub>O/CH<sub>3</sub>CH<sub>2</sub>OH for HER under a static overpotential of 40 mV over 16 h.

low overpotential of the Ru/C-H<sub>2</sub>O/CH<sub>3</sub>CH<sub>2</sub>OH is very close to that of the commercial Pt/C ( $\eta_{10} = 30$  mV) and much lower than that of the commercial Ru powder (183 mV) as well as other reported HER electrocatalysts (Table S2) [31,49,52–58]. It is believed that the chain-like porous Ru/C-H<sub>2</sub>O/CH<sub>3</sub>CH<sub>2</sub>OH catalyst provides more exposed Ru nanoparticles, which can lead to enhanced electrolyte diffusion and promoted charge transfer. Since mass activity is also important for estimating the HER catalytic ability of the as-prepared catalysts, we have provided the mass activity of Ru/C samples according to the calculated metal loadings (Fig. 3b and Table S3). The overpotential of Ru/C-H<sub>2</sub>O, Ru/C-H<sub>2</sub>O/CH<sub>3</sub>CH<sub>2</sub>OH and Ru/C-CH<sub>3</sub>CH<sub>2</sub>OH at 10 mA mg<sub>metal</sub><sup>-1</sup> are 25.1, 10.2, and 24.2 mV, respectively, which is consistent with the trend of activity based on geometric surface areas of electrodes. We have also compared the HER activity of the Ru/C-H<sub>2</sub>O/CH<sub>3</sub>CH<sub>2</sub>OH nanocomposites prepared from different time periods. Although Ru/C phase can be formed in a shorter solvothermal process (Fig. S9), but a reaction time of 3 days is optimal in terms of the overpotential at a cathodic current density of -10 mA cm<sup>-2</sup> (Fig. S10). To shed light on the catalytic kinetics of the HER process, Tafel slopes derived from the polarization curves are given in Fig. 3c. The Tafel slope of the Ru/C-H<sub>2</sub>O/CH<sub>3</sub>CH<sub>2</sub>OH (36.2 mV dec<sup>-1</sup>) is much lower than that of the Ru/C-H<sub>2</sub>O (66.8 mV dec<sup>-1</sup>), Ru/C-CH<sub>3</sub>CH<sub>2</sub>OH (56.1 mV dec<sup>-1</sup>), and commercial Ru powder (95.3 mV dec<sup>-1</sup>). Also, it is comparable to Pt/C catalyst (30.2 mV dec<sup>-1</sup>). The highly efficient kinetics for the HER on the Ru/C-H<sub>2</sub>O/CH<sub>3</sub>CH<sub>2</sub>OH catalyst suggests a Volmer-Tafel mechanism with a rate-determining step associated with electrochemical desorption of hydrogen [59–62].

Electrochemical accessible surface area (ECSA) of the studied catalysts was determined through their electrical double-layer capacitances in acidic electrolyte. To better interpret and compare the ECSA of different catalysts, CVs were recorded at a window from -0.1 to -0.2 V with different scan rates from 20 to 200 mV s<sup>-1</sup> (Fig. S11), and capacitive currents were collected at the same potential of -0.15 V (Fig. 3d). Ru/C-H<sub>2</sub>O/CH<sub>3</sub>CH<sub>2</sub>OH shows the highest specific capacitance of 3.52 mF cm<sup>-2</sup> compared to that of Ru/C-H<sub>2</sub>O (1.85 mF cm<sup>-2</sup>), Ru/C-CH<sub>3</sub>CH<sub>2</sub>OH (1.95 mF cm<sup>-2</sup>), and Ru powder (0.08 mF cm<sup>-2</sup>), suggesting that Ru/C-H<sub>2</sub>O/CH<sub>3</sub>CH<sub>2</sub>OH with more exposed Ru nanoparticles has the largest active surface area for electrochemical reactions. Electrochemical impedance spectroscopy (EIS) was carried out, from 100 kHz

to 0.1 Hz, to gain a better understanding of the HER kinetics occurring at the electrode/electrolyte interface. The Nyquist plots (Fig. 3e) were fitted using an equivalent circuit (inset in Fig. 3e) to calculate the charge transfer resistance (R<sub>ct</sub>) of 14.6, 4.4, 11.1, and 71.7 Ω for Ru/C-H<sub>2</sub>O, Ru/C-H<sub>2</sub>O/CH<sub>3</sub>CH<sub>2</sub>OH, Ru/C-CH<sub>3</sub>CH<sub>2</sub>OH, and Ru powder, respectively. This indicates an efficient charge transfer at the interfaces and improved HER kinetics for the Ru/C-H<sub>2</sub>O/CH<sub>3</sub>CH<sub>2</sub>OH catalyst. The smallest R<sub>ct</sub> may be attributed to the unique chain-like nanostructures that can facilitate the electron transfer process [63–66]. Coinciding LSV curves, using five measurements, for Ru/C-H<sub>2</sub>O/CH<sub>3</sub>CH<sub>2</sub>OH verified stability and reliability of the prepared catalyst for HER in an acidic media (Fig. S12). As the graphitization degree of the carbon materials may also influence the electrocatalytic activity, we have thermally treated the Ru/C materials at mild temperatures in order to prevent the agglomeration and Ostwald ripening of the Ru nanoparticles. It is revealed that a heat-treatment process does improve the graphitization degree of the carbon materials (Fig. S13), but the electrocatalytic HER activity is severely deteriorated at a temperature higher than 600 °C, which is very slightly improved at 500 °C (Fig. S14), an indication that the HER activity is mainly from the highly dispersed Ru nanoparticles. The stability of Ru/C-H<sub>2</sub>O/CH<sub>3</sub>CH<sub>2</sub>OH observed with LSV used a scan rate of 50 mV s for 1000 cycles from -0.2 to 0.2 V (Fig. 3f). Negligible decay is observed based on the polarization curves before and after 1000 cycles, suggesting the excellent stability of Ru/C-H<sub>2</sub>O/CH<sub>3</sub>CH<sub>2</sub>OH. The Raman spectra examined before and after 1000 cycles (Fig. S15) reveal no apparent structural and compositional change during the course of HER in acidic medium, which confirms excellent stability of Ru/C-H<sub>2</sub>O/CH<sub>3</sub>CH<sub>2</sub>OH for HER catalysis. To probe the durability of Ru/C-H<sub>2</sub>O/CH<sub>3</sub>CH<sub>2</sub>OH, chronoamperometric test at a constant potential of 40 mV in 0.5 M H<sub>2</sub>SO<sub>4</sub> was performed, which exhibits stable current density for a long period of 16 h (inset in Fig. 3f). In addition, no noticeable change in the size and morphology of Ru/C-H<sub>2</sub>O/CH<sub>3</sub>CH<sub>2</sub>OH could be seen in TEM and HRTEM images after the HER test, confirming its robustness as a highly active HER electrocatalyst (Fig. S16).

In addition to studying the HER in acidic media, Ru/C-H<sub>2</sub>O, Ru/C-H<sub>2</sub>O/CH<sub>3</sub>CH<sub>2</sub>OH, and Ru/C-CH<sub>3</sub>CH<sub>2</sub>OH are also found to be active and stable in alkaline and neutral media. As shown in Fig. S17, S18 and Table S3, compared to Ru/C-H<sub>2</sub>O and Ru/C-CH<sub>3</sub>CH<sub>2</sub>OH, Ru/C-H<sub>2</sub>O/

$\text{CH}_3\text{CH}_2\text{OH}$  generates a current density of  $-10 \text{ mA cm}^{-2}$  at a low overpotential of 53 and 93 mV in 1.0 M KOH and 3.5 wt% NaCl solution, respectively. After normalizing the electrocatalytic mass activity of all catalysts according to the metal loadings, Ru/C-H<sub>2</sub>O/CH<sub>3</sub>CH<sub>2</sub>OH has the highest mass activity among all studied catalysts, showing overpotentials of 35.2 mV in 1.0 M KOH solution and 47.6 mV in 3.5 wt% NaCl solution at  $10 \text{ mA mg}_{\text{metal}}^{-1}$ . The corresponding Tafel slopes are 47 and 108 mV dec<sup>-1</sup>, respectively. Especially in the neutral media, catalytic activity of Ru/C-H<sub>2</sub>O/CH<sub>3</sub>CH<sub>2</sub>OH for the HER is even better than that of the commercial Pt/C (157 mV at  $10 \text{ mA cm}^{-2}$  and 57.3 mV at  $10 \text{ mA mg}_{\text{metal}}^{-1}$ ) and Ru powder (106 mV at  $10 \text{ mA cm}^{-2}$  and 68.8 mV at  $10 \text{ mA mg}_{\text{metal}}^{-1}$ ). We also tested the stability of the Ru/C-H<sub>2</sub>O/CH<sub>3</sub>CH<sub>2</sub>OH in alkaline and neutral media. After continuous CV scanning for 1000 cycles at a scan rate of 50 mV s<sup>-1</sup> from -0.2 to 0.2 V, the polarization curve shows negligible loss of current density in both electrolytes (Fig. S17d and Fig. S18d), suggesting the good stability of the Ru/C-H<sub>2</sub>O/CH<sub>3</sub>CH<sub>2</sub>OH. From Raman analysis (Fig. S19) and TEM images (Fig. S20), it can be observed that the structure and morphology of the Ru/C-H<sub>2</sub>O/CH<sub>3</sub>CH<sub>2</sub>OH is generally well maintained after 1000 CV cycles.

To demonstrate the bifunctional electrocatalytic HOR/HER performance for reversible fuel cells, we also studied the HOR activity of the Ru/C-H<sub>2</sub>O, Ru/C-H<sub>2</sub>O/CH<sub>3</sub>CH<sub>2</sub>OH, Ru/C-CH<sub>3</sub>CH<sub>2</sub>OH, Ru powder, and Pt/C catalysts in acidic (0.1 M HClO<sub>4</sub>), alkaline (1 M KOH), and neutral solution (3.5 wt% NaCl) (Fig. 4, S21, S22). Fig. 4a shows the polarization curves obtained in 0.1 M KOH aqueous solution saturated with H<sub>2</sub> and using a rotation rate of 1600 rpm. The HOR current density increases up to 0.3 V and then decreases. It is worth noting that the oxidation of Ru-species would happen when the potential is positive than 0.2 V, so the peaks around 0.3 V are derived from desorption (oxidation) of underpotentially deposited hydrogen (H<sub>upd</sub>) and the Ru surface oxidation [67–70]. The onset of HOR on Ru-based catalysts are observed essentially at zero overpotential, suggesting that Ru/C have high intrinsic HOR activity in alkaline solution. Similar features are also observed in the CV curves (Fig. S23). In contrast, H<sub>upd</sub> processes in acidic electrolyte are shifted negatively compared to that in alkaline (Fig. S21), while it shifted anodically in neutral solution (Fig. S22). In

the acidic media, the earlier drop of the HOR current and the much lower maximum current density than those in alkaline suggests that Ru/C-H<sub>2</sub>O/CH<sub>3</sub>CH<sub>2</sub>OH is more poisoned in acid. Due to the early passivation of Ru/C-H<sub>2</sub>O/CH<sub>3</sub>CH<sub>2</sub>OH, the slower HOR rate of Ru/C-H<sub>2</sub>O/CH<sub>3</sub>CH<sub>2</sub>OH in acidic media than in alkaline is attributed to the site-blocking effect, which is consistent with the previous study [71]. Tafel slopes were used to determine the rate determining step for the HOR [72]. As shown in Fig. 4b, S21b and S22b, the Ru/C-H<sub>2</sub>O/CH<sub>3</sub>CH<sub>2</sub>OH catalyst exhibits the highest electrocatalytic activity towards HOR in acidic, alkaline, and neutral solution. Tafel slopes (Table S4, S5, and S6) suggest the Tafel-Volmer mechanism for the HOR in alkaline solution, with the Tafel process as the rate determining step. In acidic and neutral solution, the HOR will follow a Volmer-Heyrovsky mechanism, with the Heyrovsky process as the rate determining step. The exchange current ( $j_0$ ) was evaluated from the linear current-potential region from -0.01 to 0.01 V (inset in Fig. 4a) using the approximate Butler-Volmer equation  $j = j_0 (\eta F/RT)$ , where  $\eta$  is the applied overpotential ( $|\eta| \leq 0.02 \text{ V}$ ), and  $R$  is the gas constant [8.314 J/(mol K)], and  $F$  is the Faraday constant (96,485 C/mol). The  $j_0$  of each catalyst is presented in Table S4. Ru/C-H<sub>2</sub>O/CH<sub>3</sub>CH<sub>2</sub>OH has the largest exchange current density ( $0.65 \text{ mA cm}^{-2}$ ) among the studied Ru/C catalysts, even higher than Ru powder ( $0.14 \text{ mA cm}^{-2}$ ) and Pt/C ( $0.33 \text{ mA cm}^{-2}$ ).

The polarization curves at different rotating speeds have also been studied. The current density of the Ru/C-H<sub>2</sub>O/CH<sub>3</sub>CH<sub>2</sub>OH increases with the rotating speed increasing from 400 to 3600 rpm (Fig. 4c). This is proportional to the square root of the rotation speed ( $\omega^{-1/2}$ ) according to the Koutecky-Levich equation:

$$1/j = 1/j_k + 1/j_d \quad (1)$$

$$j_d = 0.62nFD^{2/3}\nu^{-1/6}c_0\omega^{1/2} \quad (2)$$

where  $j$  is the measured current density,  $j_k$  the kinetic current in absence of mass transfer limitations and  $j_d$  the diffusion current density. Using Eq. (2),  $j_d$  can be calculated, where  $n$  is the number of electrons transferred,  $D$  is the diffusivity of H<sub>2</sub> in the electrolyte,  $\nu$  is the kinematic viscosity of the electrolyte, and  $c_0$  is the solubility of H<sub>2</sub> in the electrolyte [73]. The intercept of the extrapolated line corresponds to

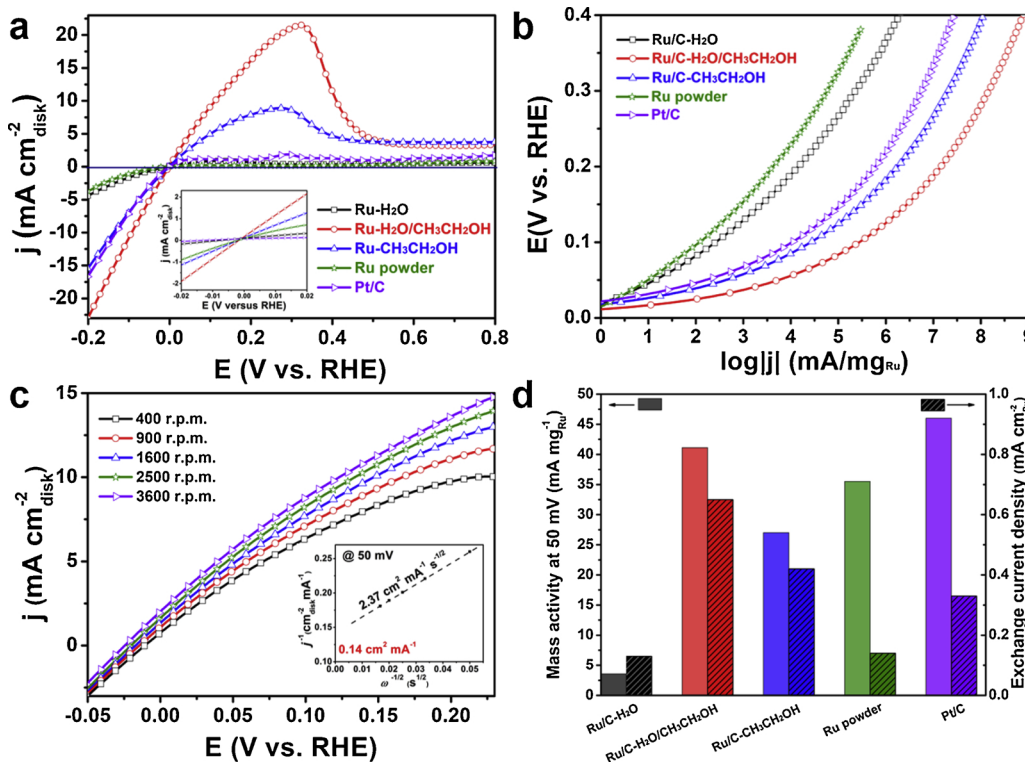


**Fig. 4.** Electrochemical characterization of the Ru/C nanoassemblies for HOR catalysis in 0.1 M KOH. (a) Polarization curves of Ru/C-H<sub>2</sub>O, Ru/C-H<sub>2</sub>O/CH<sub>3</sub>CH<sub>2</sub>OH, Ru/C-CH<sub>3</sub>CH<sub>2</sub>OH, Ru powder and Pt/C (all of the catalysts with a loading  $0.19 \pm 0.01 \text{ mg}_{\text{Ru}} \text{ cm}^{-2}$ ) in H<sub>2</sub>-saturated 0.1 M KOH at a scan rate of  $10 \text{ mV s}^{-1}$  and rotating speed of 1600 rpm. The inset shows the linear-current-potential region around the equilibrium potential for hydrogen oxidation/reduction. (b) Mass transport corrected Tafel plots in H<sub>2</sub>-saturated electrolytes. (c) Polarization curves of Ru/C-H<sub>2</sub>O/CH<sub>3</sub>CH<sub>2</sub>OH in H<sub>2</sub>-saturated 0.1 M KOH at a scan rate of  $10 \text{ mV s}^{-1}$  with various rotating speeds. Inset is the Koutecky-Levich plot at an overpotential of 50 mV. (d) Mass activity at 50 mV (unpatterned) and exchange current density (patterned) of the Ru/C-H<sub>2</sub>O, Ru/C-H<sub>2</sub>O/CH<sub>3</sub>CH<sub>2</sub>OH, Ru/C-CH<sub>3</sub>CH<sub>2</sub>OH, Ru powder and Pt/C, respectively.

the inverse of the pure kinetic current density and  $j_k$  for Ru/C-H<sub>2</sub>O/CH<sub>3</sub>CH<sub>2</sub>OH is 7.14 mA cm<sup>-2</sup> at 50 mV overpotential. The mass activities, after normalized by the metal loading of the catalyst, are 37.6 mA mg<sup>-1</sup> for the Ru/C-H<sub>2</sub>O/CH<sub>3</sub>CH<sub>2</sub>OH, which is higher than those of Ru/C-H<sub>2</sub>O (2.95 mA mg<sup>-1</sup>), Ru/C-CH<sub>3</sub>CH<sub>2</sub>OH (24.5 mA mg<sup>-1</sup>), Ru powder (35.5 mA mg<sup>-1</sup>) and Pt/C (9.21 mA mg<sup>-1</sup>) (Fig. 4d, Fig. S24 and Table S4). This mass activity of Ru/C-H<sub>2</sub>O/CH<sub>3</sub>CH<sub>2</sub>OH is comparable to the activity of Pt-based catalyst reported in the previous literature (Table S7) [74–77]. The electrochemical active surface area (ECSA) for HOR was determined by a Cu underpotential deposition (Cu<sub>upd</sub>) stripping voltammetry (Fig. S25) [67,78,79]. Among the studied electrocatalysts, Ru/C-H<sub>2</sub>O/CH<sub>3</sub>CH<sub>2</sub>OH has the highest ECSA of 47.9 m<sup>2</sup> g<sup>-1</sup>, followed by the Ru/C-CH<sub>3</sub>CH<sub>2</sub>OH (23.5 m<sup>2</sup> g<sup>-1</sup>), Ru/C-H<sub>2</sub>O (11.7 m<sup>2</sup> g<sup>-1</sup>) and Ru powder (5.1 m<sup>2</sup> g<sup>-1</sup>).

The exchange current and mass activity of all catalysts in acidic and neutral media were also calculated, and the results are shown in Fig. S21, S22 and Table S5, S6. Compared with Ru/C-H<sub>2</sub>O and Ru/C-CH<sub>3</sub>CH<sub>2</sub>OH, Ru/C-H<sub>2</sub>O/CH<sub>3</sub>CH<sub>2</sub>OH still has the highest exchange current and mass activity in 1 M KOH and 3.5 wt% NaCl solution, respectively. In addition, the stability of the Ru/C-H<sub>2</sub>O/CH<sub>3</sub>CH<sub>2</sub>OH was measured after 1000 CV cycles (Fig. S26a, S27a, and S28a). Chronoamperometry tests were carried out at a constant potential of 35, 11 and 45 mV in 0.1 M KOH, 0.1 M HClO<sub>4</sub> and 3.5 wt% NaCl solution, respectively (Fig. S26b, S27b, S28b). The negligible loss of current density indicates the good stability. Furthermore, the structure (Fig. S29) and morphology (Fig. S30) of the Ru/C-H<sub>2</sub>O/CH<sub>3</sub>CH<sub>2</sub>OH are well reserved after stability tests. The Ru/C-H<sub>2</sub>O/CH<sub>3</sub>CH<sub>2</sub>OH exhibits comparable HOR activity to the state-of-the-art Pt catalyst, which is able to replace Pt for the challenging HOR in alkaline media for alkaline fuel cell applications.

#### 4. Conclusions

In summary, we have synthesized Ru/C catalysts consisting of Ru nanoassembly supported on carbon matrix with a porous structure through a facile one-pot solvothermal method. It is revealed that Ru is formed by the self-decomposition of RuCl<sub>3</sub>·xH<sub>2</sub>O. The applied solvent plays an important role in the morphology control of the Ru/C nanocomposites. For the electrocatalytic hydrogen evolution and oxidation reactions, Ru/C-H<sub>2</sub>O/CH<sub>3</sub>CH<sub>2</sub>OH, prepared from a mixture solvent of water and ethanol, shows a Pt-like HER activity with very low overpotentials at -10 mA cm<sup>-2</sup> (35 mV in 0.5 M H<sub>2</sub>SO<sub>4</sub>, 53 mV in 1.0 M KOH, and 93 mV in 3.5 wt% NaCl), due to the chain-like and porous structure with more exposed Ru sites. Moreover, Ru/C-H<sub>2</sub>O/CH<sub>3</sub>CH<sub>2</sub>OH can also efficiently oxidize H<sub>2</sub> into H<sub>2</sub>O at all pH values with remarkably enhanced mass activity and exchange current density as comparable to that of Pt/C. This synthesis of Ru/C nanoassembly catalysts by using variable solvent provides an effective strategy to control catalyst morphology and nanostructures for improved catalytic performance. Compared to the Pt/C catalyst, the low price, high acid-resistance ability, encouraging bifunctional HER and HOR catalytic activity, as well as outstanding stability and durability of the Ru/C catalysts would offer a new opportunity to develop low-cost and durable bifunctional electrocatalysts as alternatives to the state-of-the-art noble metal-based catalysts for water electrolyzers and fuel cells.

#### Conflict of interest

We declare no conflict of interest.

#### Acknowledgements

We thank the financial support from the National Natural Science Foundation of China (21471039, 21571043, 21671047, 21871065), and Natural Science Foundation of Heilongjiang Province (B2015001). G.W. is also grateful to the support from U.S. Department of Energy,

Fuel Cell Technologies Office.

#### Appendix A. Supplementary data

Supplementary material related to this article can be found, in the online version, at doi:<https://doi.org/10.1016/j.apcatb.2019.117952>.

#### References

- [1] T. Kosmala, H. Coy Diaz, H.P. Komsa, Y. Ma, A.V. Krasheninnikov, M. Batzill, S. Agnoli, *Adv. Energy Mater.* 8 (2018) 1800031.
- [2] S. Deng, Y. Zhong, Y. Zeng, Y. Wang, X. Lu, X. Xia, J. Tu, *Adv. Sci.* 5 (2018) 1700772.
- [3] X. Han, F. Cheng, C. Chen, F. Li, J. Chen, *Inorg. Chem. Front.* 3 (2016) 866–871.
- [4] Y. Guo, J. Tang, J. Henzie, B. Jiang, H. Qian, Z. Wang, H. Tan, Y. Bando, Y. Yamauchi, *Mater. Horiz.* 4 (2017) 1171–1177.
- [5] H. Zhou, F. Yu, Y. Huang, J. Sun, Z. Zhu, R.J. Nielsen, R. He, J. Bao, W.A. Goddard, S. Chen, Z. Ren, *Nat. Commun.* 7 (2016) 12765.
- [6] K. Lei, L. Cong, X. Fu, F. Cheng, J. Chen, *Inorg. Chem. Front.* 3 (2016) 928–933.
- [7] Y. Guo, J. Tang, H. Qian, Z. Wang, Y. Yamauchi, *Chem. Mater.* 29 (2017) 5566–5573.
- [8] F. Luo, Q. Zhang, X. Yu, S. Xiao, Y. Ling, H. Hu, L. Guo, Z. Yang, L. Huang, W. Cai, H. Cheng, *Angew. Chem. Int. Ed.* 57 (2018) 14862–14867.
- [9] U.K. Sultana, J.D. Riches, A.P. Mullane, *Adv. Funct. Mater.* 28 (2018) 1804361.
- [10] T. Zhang, K. Yang, C. Wang, S. Li, Q. Zhang, X. Chang, J. Li, S. Li, S. Jia, J. Wang, L. Fu, *Adv. Energy Mater.* 8 (2018) 1801690.
- [11] G. Zhao, K. Rui, S.X. Dou, W. Sun, *Adv. Funct. Mater.* 28 (2018) 1803291.
- [12] Y. Guo, T. Park, J.W. Yi, J. Henzie, J. Kim, Z. Wang, B. Jiang, Y. Bando, Y. Sugahara, J. Tang, Y. Yamauchi, *Adv. Mater.* 31 (2019) e1807134.
- [13] L. Hui, Y. Xue, D. Jia, H. Yu, C. Zhang, Y. Li, *Adv. Energy Mater.* 8 (2018) 1800175.
- [14] B.E. Conway, J.O.M. Bockris, *J. Chem. Phys.* 26 (1957) 532–541.
- [15] P. Rüetschi, P. Delahay, *J. Chem. Phys.* 23 (1955) 195–199.
- [16] H. Tan, J. Tang, J. Henzie, Y. Li, X. Xu, T. Chen, Z. Wang, J. Wang, Y. Ide, Y. Bando, Y. Yamauchi, *ACS Nano* 12 (2018) 5674–5683.
- [17] T. Chao, X. Luo, W. Chen, B. Jiang, J. Ge, Y. Lin, G. Wu, X. Wang, Y. Hu, Z. Zhuang, Y. Wu, X. Hong, Y. Li, *Angew. Chem. Int. Ed.* 56 (2017) 16047–16051.
- [18] C.L. Bentley, C. Andronescu, M. Smialkowski, M. Kang, T. Tarnev, B. Marler, P.R. Unwin, U.P. Apfel, W. Schuhmann, *Angew. Chem. Int. Ed.* 57 (2018) 4093–4097.
- [19] J.R. McKone, E.L. Warren, M.J. Bierman, S.W. Boettcher, B.S. Brunschwig, N.S. Lewis, H.B. Gray, *Energy Environ. Sci.* 4 (2011) 3573.
- [20] H. Tan, Y. Li, J. Kim, T. Takei, Z. Wang, X. Xu, J. Wang, Y. Bando, Y.M. Kang, J. Tang, Y. Yamauchi, *Adv. Sci.* 5 (2018) 1800120.
- [21] H. Tan, Y. Li, X. Jiang, J. Tang, Z. Wang, H. Qian, P. Mei, V. Malgras, Y. Bando, Y. Yamauchi, *Nano Energy* 36 (2017) 286–294.
- [22] L. Gloag, T.M. Benedetti, S. Cheong, Y. Li, X.H. Chan, L.M. Lacroix, S.L.Y. Chang, R. Arenal, I. Florea, H. Barron, A.S. Barnard, A.M. Henning, C. Zhao, W. Schuhmann, J.J. Gooding, R.D. Tilley, *Angew. Chem. Int. Ed.* 57 (2018) 10241–10245.
- [23] T. Reier, M. Oezaslan, P. Strasser, *ACS Catal.* 2 (2012) 1765–1772.
- [24] J.X. William, J. Mitchell, T.A. Jachimowski, W.H. Weinberg, *J. Am. Chem. Soc.* 117 (1995) 2606–2617.
- [25] J. Mahmood, F. Li, S.M. Jung, M.S. Okyay, I. Ahmad, S.J. Kim, N. Park, H.Y. Jeong, J.B. Baek, *Nat. Nanotechnol.* 12 (2017) 441–446.
- [26] U. Joshi, S. Malkhandi, Y. Ren, T.L. Tan, S.Y. Chiam, B.S. Yeo, *ACS Appl. Mater. Interfaces* 10 (2018) 6354–6360.
- [27] Y. Li, F. Chu, Y. Liu, Y. Kong, Y. Tao, Y. Li, Y. Qin, *Chem. Commun.* 54 (2018) 13076–13079.
- [28] Y. Li, L.A. Zhang, Y. Qin, F. Chu, Y. Kong, Y. Tao, Y. Li, Y. Bu, D. Ding, M. Liu, *ACS Catal.* 8 (2018) 5714–5720.
- [29] P. Pachfule, X. Yang, Q.L. Zhu, N. Tsumori, T. Uchida, Q. Xu, *J. Mater. Chem. A* 5 (2017) 4835–4841.
- [30] W. Li, Y. Liu, M. Wu, X. Feng, S.A.T. Redfern, Y. Shang, X. Yong, T. Feng, K. Wu, Z. Liu, B. Li, Z. Chen, J.S. Tse, S. Lu, B. Yang, *Adv. Mater.* 30 (2018) e1800676.
- [31] P. Jiang, Y. Yang, R. Shi, G. Xia, J. Chen, J. Su, Q. Chen, *J. Mater. Chem. A* 5 (2017) 5475–5485.
- [32] J. Zhang, P. Liu, G. Wang, P.P. Zhang, X.D. Zhuang, M.W. Chen, I.M. Weidinger, X.L. Feng, *J. Mater. Chem. A* 5 (2017) 25314–25318.
- [33] Y.V. Kaneti, J. Tang, R.R. Salunkhe, X. Jiang, A. Yu, K.C. Wu, Y. Yamauchi, *Adv. Mater.* 29 (2017) 1604898.
- [34] Q. Li, P. Xu, W. Gao, S.G. Ma, G.Q. Zhang, R.G. Cao, J. Cho, H.L. Wang, G. Wu, *Adv. Mater.* 26 (2014) 1378–1386.
- [35] Q. Li, T. Wang, D. Havas, H. Zhang, P. Xu, J. Han, J. Cho, G. Wu, *Adv. Sci.* 3 (2016) 1600140.
- [36] C. Wang, S. Liu, D. Wang, Q. Chen, *J. Mater. Chem. A* 6 (2018) 11037–11043.
- [37] D. Chen, M. Huang, S. He, S. He, L. Ding, Q. Wang, S. Yu, S. Miao, *Appl. Clay Sci.* 119 (2016) 109–115.
- [38] S. Zhang, L. Li, S. Zhao, Z. Sun, J. Luo, *Inorg. Chem.* 54 (2015) 8375–8379.
- [39] W. Zhang, M. Kauer, O. Halbherr, K. Epp, P. Guo, M.I. Gonzalez, D.J. Xiao, C. Wiktor, F.X. Xamena, C. Woell, Y. Wang, M. Muhler, R.A. Fischer, *Chem-Eur. J.* 22 (2016) 14297–14307.
- [40] O. Kozachuk, K. Yusenko, H. Noei, Y. Wang, S. Walleck, T. Glaser, R.A. Fischer, *Chem. Commun.* 47 (2011) 8509–8511.

[41] W. Zhang, K. Freitag, S. Wannapaiboon, C. Schneider, K. Epp, G. Kieslich, R.A. Fischer, Inorg. Chem. 55 (2016) 12492–12495.

[42] Y. Wu, H. Chen, J. Xiao, D. Liu, Z. Liu, Y. Qian, H. Xi, ACS Appl. Mater. Interfaces 7 (2015) 26930–26940.

[43] R. Jin, Q. Zhai, Q. Wang, Chem. Eur. J. 23 (2017) 14056–14063.

[44] Y.Z. He, P. Xu, B. Zhang, Y.C. Du, B. Song, X.J. Han, H.S. Peng, ACS Appl. Mater. Interfaces 9 (2017) 38401–38408.

[45] J.L. He, Y.Z. He, Y.N. Fan, B. Zhang, Y.C. Du, J.Y. Wang, P. Xu, Carbon 124 (2017) 630–636.

[46] T.K. Sham, Richard J. Puddephatt, Jayasree Sankar, J. Mater. Chem. A 9 (1999) 2439–2444.

[47] H. Noei, O. Kozachuk, S. Amirjalayer, S. Bureekaew, M. Kauer, R. Schmid, B. Marler, M. Muhler, R.A. Fischer, Y. Wang, J. Phys. Chem. C. 117 (2013) 5658–5666.

[48] N. Hamzah, N.M. Nordin, A.H.A. Nadzri, Y.A. Nik, M.B. Kassim, M.A. Yarmo, Appl. Catal. A 419–420 (2012) 133–141.

[49] S. Drouet, J. Creus, V. Colliere, C. Amiens, J. Garcia-Anton, X. Sala, K. Philippot, Chem. Commun. 53 (2017) 11713–11716.

[50] H. Zhang, Z. Ma, J. Duan, H. Liu, G. Liu, T. Wang, K. Chang, M. Li, L. Shi, X. Meng, K. Wu, J. Ye, ACS Nano 10 (2016) 684–694.

[51] Y. Liu, X. Yong, Z. Liu, Z. Chen, Z. Kang, S. Lu, Adv. Sustainable Syst. 3 (2019) 1800161.

[52] E. Demir, S. Akbayrak, A.M. Onal, S. Ozkar, ACS Appl. Mater. Interfaces 10 (2018) 6299–6308.

[53] Z. Pu, I.S. Amiinu, Z. Kou, W. Li, S. Mu, Angew. Chem. Int. Ed. 56 (2017) 11559–11564.

[54] R. Ye, Y. Liu, Z. Peng, T. Wang, A.S. Jalilov, B.I. Yakobson, S.H. Wei, J.M. Tour, ACS Appl. Mater. Interfaces 9 (2017) 3785–3791.

[55] L.X. Chen, Z.W. Chen, Y. Wang, C.C. Yang, Q. Jiang, ACS Catal. 8 (2018) 8107–8114.

[56] Y. Wu, F. Li, W. Chen, Q. Xiang, Y. Ma, H. Zhu, P. Tao, C. Song, W. Shang, T. Deng, J. Wu, Adv. Mater. 30 (2018) e1803151.

[57] Y. Yin, Y. Zhang, T. Gao, T. Yao, X. Zhang, J. Han, X. Wang, Z. Zhang, P. Xu, P. Zhang, X. Cao, B. Song, S. Jin, Adv. Mater. 29 (2017) 1700311.

[58] B. Song, K. Li, Y. Yin, T. Wu, L. Dang, M. Caban-Acevedo, J. Han, T. Gao, X. Wang, Z. Zhang, J.R. Schmidt, P. Xu, S. Jin, ACS Catal. 7 (2017) 8549–8557.

[59] X. Xiao, D. Huang, Y. Fu, M. Wen, X. Jiang, X. Lv, M. Li, L. Gao, S. Liu, M. Wang, C. Zhao, Y. Shen, ACS Appl. Mater. Interfaces 10 (2018) 4689–4696.

[60] Y. Yin, J. Han, Y. Zhang, X. Zhang, P. Xu, Q. Yuan, L. Samad, X. Wang, Y. Wang, Z. Zhang, P. Zhang, X. Cao, B. Song, S. Jin, J. Am. Chem. Soc. 138 (2016) 7965–7972.

[61] X. Li, J. Wei, Q. Li, S. Zheng, Y. Xu, P. Du, C. Chen, J. Zhao, H. Xue, Q. Xu, H. Pang, Adv. Funct. Mater. 28 (2018) 1800886.

[62] Z. Wei, Y. Liu, Z. Peng, H. Song, Z. Liu, B. Liu, B. Li, B. Yang, S. Lu, ACS Sustain. Chem. Eng. 7 (2019) 7014–7023.

[63] P. Ge, S. Li, H. Shuai, W. Xu, Y. Tian, L. Yang, G. Zou, H. Hou, X. Ji, Nano Energy 54 (2018) 26–38.

[64] C. He, T. Bo, B. Wang, J. Tao, Nano Energy 62 (2019) 85–93.

[65] Y.L. Zhang, X.L. Sui, L. Zhao, D.M. Gu, G.S. Huang, Z.B. Wang, Int. J. Hydrogen Energy 44 (2019) 6551–6559.

[66] W. Zhang, X. Yao, S. Zhou, X. Li, L. Li, Z. Yu, L. Gu, Small 14 (2018) e1800423.

[67] T.S. Ohyama, Y. Yamamoto, S. Arai, A. Satsuma, J. Am. Chem. Soc. 135 (2013) 8016–8021.

[68] H.A.M. Gasteiger, N.M. Ross, J. Phys. Chem. 99 (1995) 8290.

[69] H.W. Inoue, J.X. Sasaki, K. Adzic, J. Electroanal. Chem. 77 (2003) 554–555.

[70] Q. Li, H. Peng, Y. Wang, L. Xiao, J. Lu, L. Zhuang, Angew. Chem. Int. Ed. 58 (2019) 1442–1446.

[71] N. Ramaswamy, S. Ghoshal, M.K. Bates, Q. Jia, J. Li, S. Mukerjee, Nano Energy 41 (2017) 765–771.

[72] B.V. Tilak, B.E. Conway, Electrochim. Acta 47 (2002) 3571–3594.

[73] S.T.S. Nenad, M. Marković, A. Gasteiger, N. Ross, J. Chem. Soc. Faraday Trans. 92 (1996) 3719–3725.

[74] Z. Zhuang, S.A. Giles, J. Zheng, G.R. Jenness, S. Caratzoulas, D.G. Vlachos, Y. Yan, Nat. Commun. 7 (2016) 10141.

[75] D. Strmcnik, M. Uchimura, C. Wang, R. Subbaraman, N. Danilovic, D. Vliet, A.P. Paulikas, V.R. Stamenkovic, N.M. Markovic, Nat. Chem. 5 (2013) 300–306.

[76] J. Durst, A. Siebel, C. Simon, F. Hasché, J. Herranz, H.A. Gasteiger, Energy Environ. Sci. 7 (2014) 2255–2260.

[77] J. Zheng, W. Sheng, Z. Zhuang, B. Xu, Y. Yan, Sci. Adv. 2 (2016) e1501602.

[78] F. Tzorbatzoglou, A. Brouzgou, S. Jing, Y. Wang, S. Song, P. Tsakaras, Int. J. Hydrogen Energy 43 (2018) 11766–11777.

[79] H. Begum, M.S. Ahmed, S. Jeon, ACS Appl. Mater. Interfaces 9 (2017) 39303–39311.